ADVANCED ELECTRONIC MATERIALS
www.advelectronicmat.de

Growing Perovskite Quantum Dots on Carbon Nanotubes for Neuromorphic Optoelectronic Computing

Jinxin Li, Priyanka Dwivedi, Kowsik Sambath Kumar, Tania Roy, Kaitlyn E. Crawford, and Jayan Thomas**

Brain-inspired (neuromorphic) computing that offers lower energy consumption and parallelism (simultaneous processing and memorizing) compared to von Neumann computing provides excellent opportunities in many computational tasks ranging from image recognition to speech processing. To accomplish neuromorphic computing, highly efficient optoelectronic synapses, which can be the building blocks of optoelectronic neuromorphic computers, are necessary. Currently, carbon nanotubes (CNTs), an attractive candidate to develop circuit-level photonic synapses, provide weak light responses. The inferior photoresponse of CNTs increases the energy consumption of neuromorphic optoelectronic devices. Herein, a method to grow organic–inorganic halide perovskite quantum dots (PQDs) directly on multiwall CNTs (MWCNTs) to increase the photosensitivity of optoelectronic synapses is demonstrated. The new hybrid material synchronizes the high photoresponse of PQDs and the excellent electrical properties of MWCNTs to provide photonic memory under very low light intensity (125 µW cm^{-2}). However, neat MWCNTs do not show any detectable light response at the tested light intensity, as high as 25 mW cm^{-2}. Since the PQDs are grown directly on and in the MWCNTs, the hybrid PQD-MWCNT provides a new direction for the future MWCNT-based optoelectronic devices for neuromorphic computing with a potential to break the von Neumann bottleneck.

1. Introduction

The traditional computing system, which is based on von Neumann architecture, has demonstrated its power in solving problems related to well-formulated mathematical calculations. Due to the physical separation of the calculation (processing) unit and the data storage (memory) unit, the architecture has an energy efficiency limit for high-speed data processing.[1] Instead, neuromorphic computing, also called brain-inspired computing, consumes low energy because the building block has the ability to simultaneously memorize and process the data.[2] Currently, artificial neural networks show strength in complicated computational machine learning tasks such as image recognition,[3] audio recognition,[4] protein structure revealing, and material discovery.[5] These machine learning tasks rely on a large volume of data and high-speed data analysis. Therefore, compared to the traditional von Neumann architecture, brain-inspired computing architecture that mimics the basic elements of the biological brain—neurons and synapses—are emerging as a computing solution for complicated machine learning tasks. Among the component devices for the realization of neuromorphic computing, optoelectronic devices, which can act as building blocks of optoelectronic neuromorphic computers, need novel materials to make circuit-level and nanoscale level devices.

Carbon nanotubes (CNTs) are commonly used in electronic devices because of their excellent mechanical and electrical properties.[6] Unlike 2D graphene materials that are used in devices as single or multilayer films, 1D CNTs have better potential for use in circuit-level and nanoscale device applications. As a an electrical material with high carrier mobility, CNTs are used to build field-effect transistors and computers.[7] Despite the excellent electrical properties of CNTs (including multiwall CNTs (MWCNTs)), their response to light is weak and are not suitable

J. Li
CREOL, The College of Optics and Photonics
NanoScience Technology Center
University of Central Florida
Orlando, FL 32816, USA

Dr. P. Dwivedi, K. S. Kumar, Prof. T. Roy
NanoScience Technology Center
Department of Materials Science and Engineering
University of Central Florida
Orlando, FL 32816, USA

The ORCID identification number(s) for the author(s) of this article can be found under https://doi.org/10.1002/aelm.202000535.

DOI: 10.1002/aelm.202000535

Prof. K. E. Crawford
Department of Materials Science and Engineering
NanoScience Technology Center
Department of Chemistry
Biionix Cluster
University of Central Florida
Orlando, FL 32816, USA
E-mail: KCrawford@ucf.edu

Prof. J. Thomas
NanoScience Technology Center
Department of Materials Science and Engineering
CREOL
The College of Optics and Photonics
University of Central Florida
Orlando, FL 32816, USA
E-mail: Jayan.Thomas@ucf.edu

© 2020 Wiley-VCH GmbH

for many optoelectronic applications on their own. Recently, Agnus et al. used MWCNTs to realize photonic memory, but the light intensity used was as high as 40 W cm^{-2}.[8] This inferior light response motivates researchers to develop various approaches to improve the photoresponse.[9] Unlike the current bilayer approach of depositing a light sensitive material like quantum dots (QDs) on top of a CNT layer,[9c,d] if QDs are grown on individual CNTs, it can lead to the development of a single CNT level optoelectronic device. A recently published paper reports the preparation of perovskite quantum dots (PQDs) on SWCNTs by just mixing PQDs with SWCNTs.[10] Since PQDs and CNTs are just mixed together, i.e., PQDs are not grown on SWCNTs, they observed only a three times enhancement of the light response for a drop casted film prepared without following any washing procedure.

Organic–inorganic halide PQDs are attractive candidates for optoelectronic devices because they are good photocarrier generators, have high light absorption, good bandgap tunability, and easy fabrication. PQDs are used in advancing technologies such as solar cells,[11] photodetectors,[12] and memory devices.[13] Recent reports show that photonic memory is possible in PQD systems, such as graphene-PQD[14] and inorganic $CsPbBr_3$ PQD film.[15] However, in most of these cases, an external gate voltage is required to manipulate the photonic memory effect.

Here, we propose a novel method that combines the photoresponse of PQDs and electrical properties of MWCNTs, by growing PQDs directly on and from MWCNTs, without the need for an external gate voltage. Compared to other CNT devices that require very high light intensity to achieve a photoresponse,[8] the hybrid PQD-MWCNT based device requires only low light intensity to achieve a significant increase in light response and photonic memory. We use single and multiple light pulses to stimulate the PQD-MWCNT device to demonstrate its potential for optoelectronic brain-inspired computing applications. As a result of the unique PQD-MWCNT structural architecture, this work represents a significant step forward toward achieving nanoscale and single MWCNT optoelectronic neuromorphic devices that could one-day function as the channel for a two-terminal nanodevice.

2. Results and Discussion

In this work, we use the heterogeneous nucleation approach[14] to grow PQDs on MWCNTs. MWCNTs with a diameter of about 20 nm is presumed to be more compatible for growing PQDs with a size of 3–7 nm,[16] in comparison with single-wall CNTs (SWCNTs) of about 3 nm diameter. The details of the material fabrication are provided in the Experimental Section. Briefly, a $MAPbBr_3$ (methylammonium lead tribromide) PQD precursor solution (17.3 mg MABr + 73 mg $PbBr_2$ + 5 mL *N,N*-Dimethylformamide (DMF) + 300 µL butylamine + 500 µL oleic acid) is mixed vigorously with MWCNTs in toluene solution to generate numerous fine droplets.[17] The PQD precursor droplets then collide with the MWCNT surface, initiating heterogeneous nucleation and subsequent growth of PQDs from the MWCNT lattice (**Figure 1**a). The PQDs can overcome the activation free energy for stable nucleation and crystal growth because of the high Gibbs free surface energy of the MWCNTs surface, particularly at defect sites.

The PQD-MWCNT hybrid material was initially characterized by transmission electron microscopy (TEM) (Figure 1b,c). Figure 1b shows the PQDs randomly grown on MWCNTs and Figure 1c is the zoom image which shows PQDs grown along MWCNTs. Figure S1a in the Supporting Information is a TEM image of the hybrid material, which clearly shows the crystal structure of the PQDs. The lattice spacing of PQDs on MWCNTs is about 0.26 nm. Considering the heterogeneous nucleation method, the PQD size variation may be due to different Gibbs surface free energy of various sites on MWCNTs.[18] Absorption and photoluminescence (PL) experiments further confirm that the PQDs have different sizes (Figures 1d,e). Some small PQDs may have grown inside the channel of MWCNTs (Figure S1b, Supporting Information). We assume that these PQDs are grown inside the MWCNT channel because the edges of MWCNT and the PQD were almost at the same focal plane as we tuned the focus of the electron beam of TEM. However, there are currently no methods to confirm the growth of PQDs within the channel.

The presence of PQDs on MWCNTs can also be understood from the optical absorption and PL characteristics. Figure 1d shows the absorption spectra of the MWCNT film on glass and PQD-MWCNT film on the glass (solution absorption spectra with similar findings for both materials in toluene are in Figure S2, Supporting Information). The baseline correction of the absorption spectra is done with bare glass substrates. In the absorption spectrum of PQD-MWCNT on glass, two peaks at 437 and 453 nm could be seen, which are the absorption peaks of PQDs grown on MWCNTs. These absorption peaks are likely due to the different sizes of the PQDs[19] grown from MWCNTs. The PL spectra, at 405 nm excitation, of the same PQD-MWCNT sample yields mainly two PL peaks, 475 and 530 nm that correlate to bandgaps of 2.4 and 2.6 eV, respectively (Figure 1e). The smaller peaks between 475 and 530 nm should correspond to different PQD sizes grown on MWCNTs.

Raman spectroscopy was carried out on films of PQD, MWCNT, and PQD-MWCNT on silicon substrates using 514 nm excitation wavelength (**Figure 2**a). The Raman peak at around 520 cm^{-1} is from the signal due to the silicon substrate in all the samples. The peaks at 1347 and 1576 cm^{-1} of MWCNT matches well with the published data from the vendor.[20] The Raman peaks of $MAPbBr_3$ PQDs at 970, 1438, and 1465 cm^{-1} are very close to the reported values.[21] It can be seen that the Raman spectrum of our PQD-MWCNT is overlapped and different from those of the individual MWCNTs and PQDs. When QDs size vary, the Raman peak position could shift due to the quantum effect and surface effect.[22] Also, unlike bulk material, the Raman spectrum of QDs could be broadened due to phonon confinement effect.[23] Overall, the broad Raman spectrum of PQD-MWCNT may stem from the complicated vibrational modes and phonon confinement that results from the different sizes of QDs and the attachment of PQDs to MWCNTs.

The X-Ray diffraction (XRD) patterns of MWCNT, PQD, and PQD-MWCNT materials are shown in Figure 2b. The characteristic peak of MWCNT appeared at 2θ of 26.00° corresponding to (002) crystal planes. The formation of orthorhombic $MAPbBr_3$ QDs is confirmed by the presence of the characteristic diffraction peaks at 2θ of 15.1°, 25.9°, 27.2°, 30.16°, and 31.5° corresponding to (101), (131), (040), and (212) crystal planes, respectively.[24] The peak seen at 17.9° can be attributed to the presence of excess

© 2020 Wiley-VCH GmbH

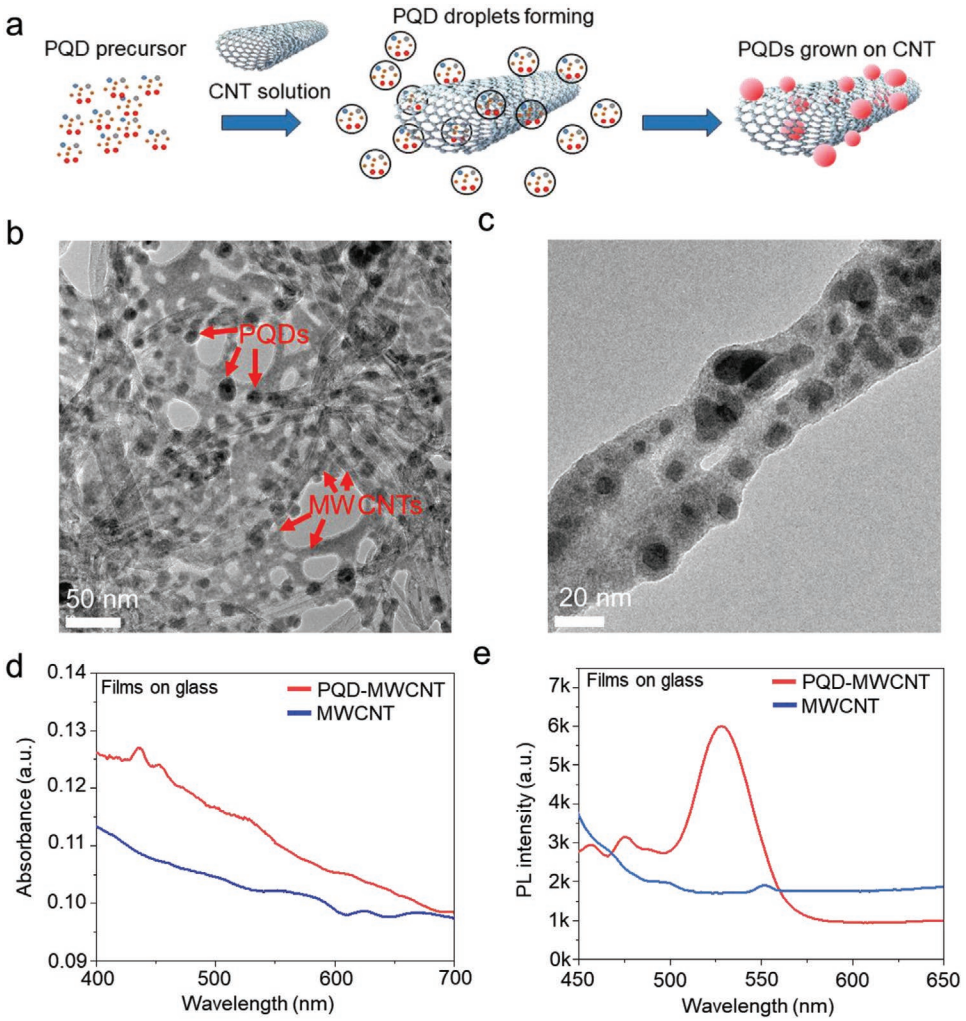

Figure 1. a) Schematic showing the formation of hybrid PQD-MWCNT. b,c) TEM images of PQD-MWCNT. d) Absorption spectra of MWCNT and PQD-MWCNT film on glass. e) PL spectra of MWCNT and PQD-MWCNT films on glass.

$PbBr_2$ from the precursor solution.[25] The XRD pattern of PQD-MWCNT clearly exhibits the characteristic peaks of $MAPbBr_3$ QDs confirming the growth of the QDs on CNT and the high intensity of QD peaks confirm the crystalline nature of the composite formed. The MWCNT peak lies in the noise level of the high intense QD peaks. A comparison of XRD for CNT and QDs on CNT is given in Figure S3 in the Supporting Information.

After the formation of the PQD-MWCNT hybrid material, we tested its photonic memory by fabricating two-terminal optoelectronic synapses without gate terminals. Our device has only two gold electrodes as terminals, which is different from other optoelectronic synapses with an add-on gate.[8,15] We fabricated our device on SiO_2/Si, which just functions as a substrate. The device consists of Au terminals that are separated by a PQD-MWCNT film (Figure 2c). In all the experiments with light, the entire device area is illuminated.

The light responses of our PQD-MWCNT device and neat MWCNT device under different wavelengths are shown in Figure 2d. The devices are illuminated for 6 s under a bias voltage of 0.5 V between two electrodes. The same applied voltage is used for all the experiments unless otherwise mentioned. For comparison, the data baseline is shifted to match for the PQD-MWCNT and MWCNT devices. To compare light response at different wavelengths, all curves for the PQD-MWCNT devices are normalized with its incident light intensity at different wavelengths. There was no light response for the device with only MWCNTs (at a light intensity of 25 mW cm^{-2}, which is the maximum output from our light source; 405 nm). In contrast, our hybrid PQD-MWCNT material shows significantly high photoresponse with orders of magnitude lower intensity than 40 W cm^{-2} at 457 nm light required to get a reasonable response as reported previously for neat CNTs.[8] Because the PQDs are known excellent photocarrier generators,[14] the significant improvement in photoresponse for the PQD-MWCNT system is attributed to the presence of PQDs grown on MWCNTs. It could be seen that 405 nm gives the maximum light response. The device shows almost no light response at 650 nm. Among the three wavelengths used (405, 532, and 650 nm), 405 nm shows the highest light response as well as the best photonic memory effect. The *I–V* curves of our PQD-MWCNT device under dark and 405 nm light are shown in Figure S4 in the Supporting Information. The *I–V* curves indicate that our device has an ohmic behavior without hysteresis.

© 2020 Wiley-VCH GmbH

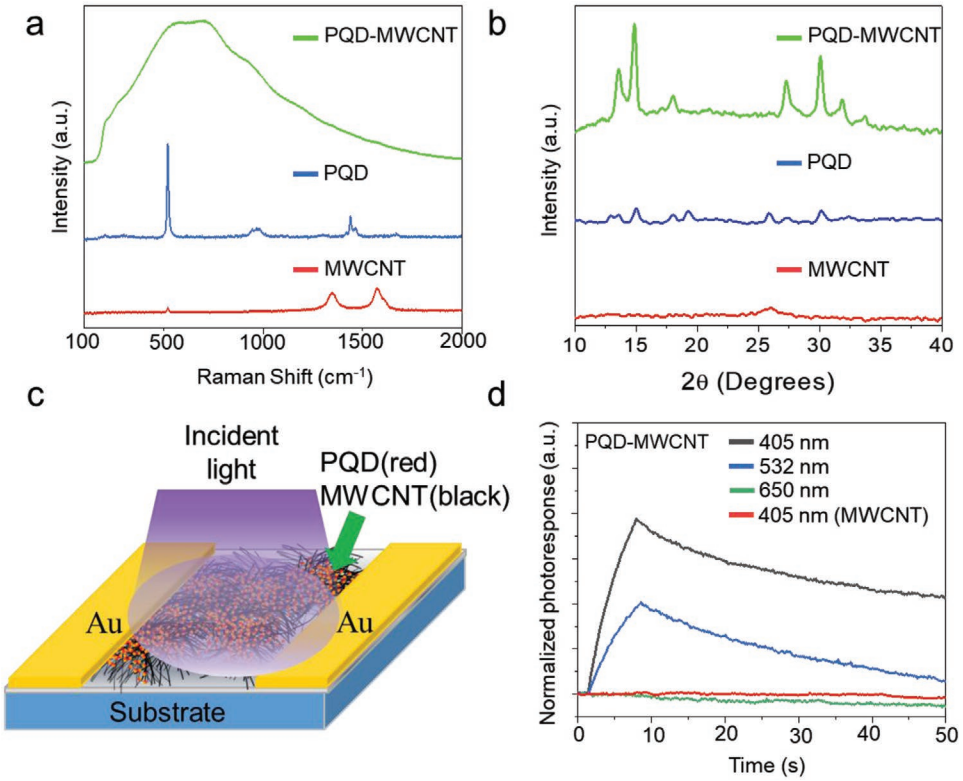

Figure 2. a) Raman spectra of PQD-MWCNT, PQD, and MWCNT films on silicon. Excitation of 514 nm laser source. b) XRD spectra of PQD-MWCNT, PQD, and MWCNT films on silicon. c) The device schematic of photonic synapse device. d) Normalized photoresponse of PQD-MWCNT photonic synapse devices under different excitation wavelengths.

In biology, synapses are the functional links between the two neurons. When the presynaptic neuron gets excited by an environmental signal, it releases different amounts of neurotransmitters into the synaptic gap based on the different intensity of excitations. In general, once in the synaptic gap, the neurotransmitters diffuse to the postsynaptic neuron. The postsynaptic current value (in comparison to the presynaptic current) is an indicator of the synapse connection strength. For our bioinspired optoelectronic synapse, light and electrical stimuli are a synapse analog to control the pseudo postsynaptic current. We examined the retention properties of our PQD-MWCNT device under different light intensities: 0.6, 0.3, 0.25, and 0.125 mW cm^{-2}, with 405 nm wavelength of pulsed light (single pulse with 5 s duration) (**Figure 3**a). Unlike other figures in Figure 3, in Figure 3a,c, ΔI (change in current) which is the current induced from light, is used to show a better comparison among different data sets. Under light stimuli of different intensities, the photonic memory strength is different (i.e., postsynaptic current strength in a biological system). It is analogous to biological synapse where different presynaptic signals can influence the synapse connection strength.

Another aspect that is analogous to the biological synapse is that the device transfers from short-term memory to long-term memory after light is turned off. In biology, short-term memory is a temporal memory that has a synapse connection strength that rapidly diminishes and thus has a small synaptic weight. In contrast, long-term memory has a temporal memory synapse connection strength that diminishes much more slowly. In our optoelectronic experiments, as shown in Figure 3a, immediately following the light stimulus (single pulse with 5 s duration), the current of our device increases rapidly when the light is on and then decreases rapidly after the light is off over tens of seconds, resembling short-term memory. After several seconds of rapid signal decay, the current stabilizes, decreasing at a much slower rate, suggesting our device transits from short-term memory to long-term memory.

To further investigate the short-term memory effects of our PQD-MWCNT optoelectronic synapse, we evaluated the pair pulse facilitation (PPF) property of our device (Figure 3b). The PPF index is described by the ratio between the postsynaptic currents of the second light pulse and the first light pulse. In Figure 3b, we applied two identical 5 s light pulses to the device (0.125 mW cm^{-2} with 405 nm light). After the first 5 s pulse stimulus, the second 5 s pulse comes after 10 s and enhances the short-term memory and synaptic connection strength. The inset of Figure 3b is obtained with exponential fitting by varying the interval of the two pulses and calculating the PPF index. PPF index increases when the interval is short, which is due to the undiminished short-term photonic memory from photogenerated carriers from the first light pulse.[15] The second light stimulus provides more photogenerated carriers that results in an increased device conductance. The PPF experiment results demonstrate that memory could be enhanced when repetitive training is performed, which is similar to how the brain memorizes new things. Therefore, when the device is trained with multiple light pulses, the learning effect in the device can be enhanced.

© 2020 Wiley-VCH GmbH

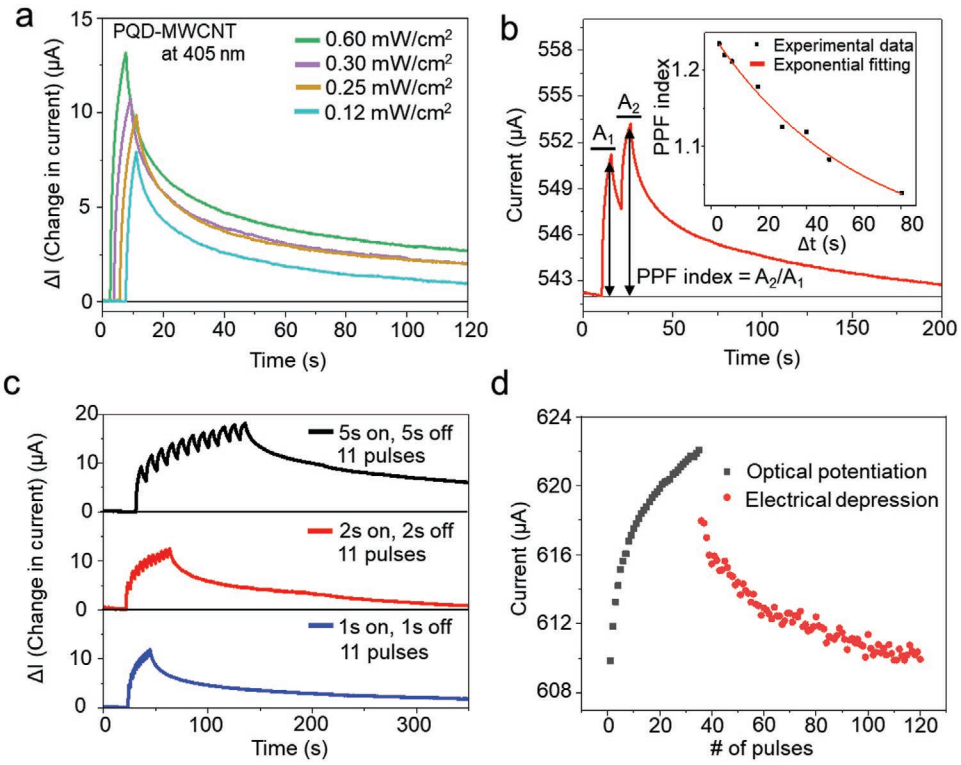

Figure 3. a) Photoresponses of the PQD-MWCNT photonic synapse devices at different intensities of 405 nm light. b) PPF index measurement. The inset figure is PPF index with respect to time interval between two pulses. c) Photonic memory of the device after different duration of 11 light pulses. d) Light potentiation and electrical depression to change the synaptic weight of the device.

In the biological brain, learning is achieved by adjusting the synaptic connection strength, which needs transition from short-term plasticity (STP) to long-term plasticity (LTP). Analogous to biological systems, the transition from STP to LTP could be achieved by applying pulse trains of stimulus that persistently increases the connection strength (i.e., synaptic weight). To evaluate the learning capabilities of our device, we applied pulse trains with 0.125 mW cm^{-2} intensity and increasing pulse durations at 405 nm light. The photonic memory transits from short-term memory to long-term memory after some time, similar to photoresponse in Figure 3a. For longer duration light pulses, it is easier for the device to saturate than with the same number of shorter pulses. The sooner the device saturates with light pulses, the more the device exhibits nonlinear behavior. For neuromorphic computing, nonlinearity is an important parameter that can affect the accuracy of pattern recognition tasks.[26] Ideally, linear synaptic weight increase with pulse stimulus is preferred. However, due to photoresponse saturation, the synaptic weight could not increase linearly. For the same number of pulses, the nonlinearity of 1 s pulse duration is smaller than that of 5 s pulse duration. Also, when longer pulses are used to stimulate the device, the number of states the device could achieve will be smaller due to the saturation of the photoresponse. Since we can regard the number of states of the device as the number of bits the device could have, a smaller number of states is not preferred for a single device to memorize complicated knowledge. We also applied more pulses with shorter pulse durations (Figures S5 and S6, Supporting Information). Figure S5 in the Supporting Information shows 2 and 5 s pulse duration with 25 pulses, in which the nonlinear weight change could be clearly seen compared to Figure 3c. LTP observation were also recorded over longer periods with over 800 s photonic memory to exemplify further trends in LTP of the devices (Figure S8, Supporting Information). It is better to mention that the photoresponse time could be affected by light wavelength, light intensity and light pulse width, which is similar to other photodetector devices. Since the dynamic range (on/off) ratio is important for synapses in neuromorphic computers, a dark current deduction unit might be preferred after our device in practical applications to realize a large dynamic range. The energy consumption per synaptic event of optically stimulated synaptic device is calculated using the relation[27]

$$dE = S \times P \times dt \tag{1}$$

where S is the area of the device, P is the input light intensity, and dt is the pulse duration of a single light pulse. For our device, the energy needed for potentiation is 6.09 nJ for a pulse duration of 0.39 s. A table comparing the energy consumption of our devices with other optoelectronic synapses is given in Table S1 in the Supporting Information.

In real biological systems, the learning process needs not only synaptic connection strength-enhancing but also strength-weakening. As stated previously, the neurotransmitters released by the presynaptic neuron diffuse to the postsynaptic neuron. The postsynaptic neuron can be either excited or inhibited due to different neurotransmitters and receptors. Therefore, our optoelectronic synapse should also be able to mimic both biological

© 2020 Wiley-VCH GmbH

potentiation (synaptic weight increases; enhancing) and depression (synaptic weight decreases; weakening). In our device, light pulses are used to potentiate the device to achieve excitatory postsynaptic current, and electrical pulses are used to depress the device to achieve inhibitory postsynaptic current.[28] The depression process is realized by electrical pulses applied to the two gold electrodes. The potentiated current is from the trapped charges in the defects, ligands and the interface between PQDs and MWCNTs. Once large negative bias pulses are applied, these trapping sites will release charges from their positions and the depression process will happen. In Figure 3d, potentiation is realized by applying 405 nm light pulse trains (0.125 mW cm^{-2} intensity) with each light pulse duration of 0.375 s and pulse period of 0.75 s, and the depression is realized by applying –1 V electrical pulses with each pulse width of 0.1 s and pulse period of 1 s. After the electrical pulse depression, the strengthened synaptic connection could be weakened. By increasing the electrical pulse width, the synaptic weight can be weakened faster (Figure 3d and Figure S7, Supporting Information). In a second experiment, 35 light pulses are applied for potentiation, but with 0.1 s pulse width, 120 electrical pulses are required to depress the device to the initial current level while only 80 electrical pulses with 0.5 s pulse width is needed to do the same. This result suggests the feasibility of neuromorphic computing to train the neural network by varying widths of pulses to adjust the speed of the learning process. The potentiation and depression ability is what allows the device to be considered as a potential synapse for optoelectronic neuromorphic computing.

The photonic memory of our device may be explained by the trapped photocarriers in the PQD-MWCNT device. There are three general regions where charge trapping may take place: defects in the PQDs and MWCNTs, ligands attached to PQDs, and traps at the interface between the PQDs and the MWCNT. The short-term memory is due to the electrons in shallow traps, while the long-term memory is likely due to those in deeper traps. In our previous work[14] where PQDs are grown on graphene, the optoelectronic synapses did not show any memory effect without gate voltage (i.e., gate voltage is required to observe memory effects). In the present work, PQD-MWCNT shows clear photonic memory without any gate voltage. There are two overarching reasons why the PQD-MWCNT hybrid material exhibits photonic memory in the absence of gate voltage. First, MWCNTs have more defects[29] compared to graphene, so the charges trapped in the MWCNT defects[30] are more compared to graphene. Second, the charges trapped at the interface between PQDs and the MWCNT may provide a good photonic memory effect. The interface charge blocking results from the band bending due to the difference in the work functions of the materials. To investigate the influence of work function, we performed Kelvin probe force microscopy (KPFM) to determine the work functions and surface potential of our MWCNT, PQD, and PQD-MWCNT samples (**Figure 4**a–c) (the first row: atomic force microscopy (AFM) images; the second row: corresponding KPFM images; the third row: calculated work functions). The surface topography of the materials were recorded in ambient conditions by AFM. KPFM measurements were performed using a two-pass method. During the first pass, the cantilever was mechanically driven at its resonant frequency to determine the topography of the sample. During the second-pass, the cantilever was lifted by a fixed distance (20 nm) to minimize the effect of short-range van der Waals forces and maximize the effect of long-range forces. The tip's work function (Φ_{tip}) is initially measured by scanning a material of known work function: a freshly exfoliated surface of highly oriented pyrolytic graphite (HOPG; Φ_{HOPG} = 4.6 eV). Scanning the HOPG's surface provides the contact potential difference (V_{CPD}) between the tip and the HOPG. Using the relation, $\Phi_{HOPG} = \Phi_{tip} - eV_{CPD}$, where e is the electronic charge, Φ_{tip} is 4.73 eV. The samples (PQD, MWCNT and PQD-MWCNT) mounted on a metallic disc were then scanned in an area of 1 μm × 1 μm at a scan rate of 1 Hz. Each sample was scanned at three different positions to confirm the work function value of the sample (Φ_{sample}). The scanning provides the V_{CPD} recorded between the tip and the sample. Using the relation, $\Phi_{sample} = \Phi_{tip} - eV_{CPD}$,[31] Φ_{sample} is measured. The work function of MWCNT is ≈4.75 eV and that of PQDs is ≈4.50 eV (Figure 4a,b). Figure 4c further demonstrates that our PQD-MWCNT is a hybrid material that shows a work function between PQDs and MWCNTs.

Due to the difference in the work functions between the MWCNT and PQDs, the Fermi energy levels need to be aligned at the growth interface (Figure 4d). The band of two materials bends generating an internal electrical potential. The internal electrical potential makes the light-induced holes move to the MWCNT side, while the electrons are trapped in the PQDs. The light-induced holes contribute to the increased current of the device. Since the photogenerated electrons are blocked at the interface and cannot move into the MWCNT to recombine with the photogenerated holes, the photonic memory develops. Based on this result, it can be predicted that the larger the band bending at the interface, the better the ability of the interface to trap photocarriers. Unlike neat graphene with a work function around 4.56 eV,[14] the Fermi energy level difference between MWCNT and PQD is much more than that between graphene and PQDs, and more photogenerated electrons could be trapped at the interface. This phenomenon further supports why PQD-graphene does not show any photonic memory under zero gate voltage;[14] meaning that the Fermi energy level difference of the two materials is important for better memory effect. The larger the Fermi energy level difference is, the longer the photonic memory of the device might be.

To demonstrate that our device could act as a synaptic building block in optoelectronic neuromorphic computers, pattern recognition is simulated by using our device as synapses between input and output neurons (**Figure 5**b). Here, from modified National Institute of Standards and Technology dataset (a well-known handwritten dataset in machine learning (ML)), we chose 2000 figures as the training set and 500 figures different from the training set as the test set. For our pattern recognition application, the fitted conductance curve of the device is shown in Figure S9 in the Supporting Information after baseline correction. The fitting parameters are shown in Table S2 in the Supporting Information. The fitting represents how our devices change synaptic weight during the training process in the simulation. In our simulation, a spiking neural network is constructed to perform unsupervised machine learning tasks similar to our previous work.[14] The details of the simulation are discussed in the Supporting Information.

© 2020 Wiley-VCH GmbH

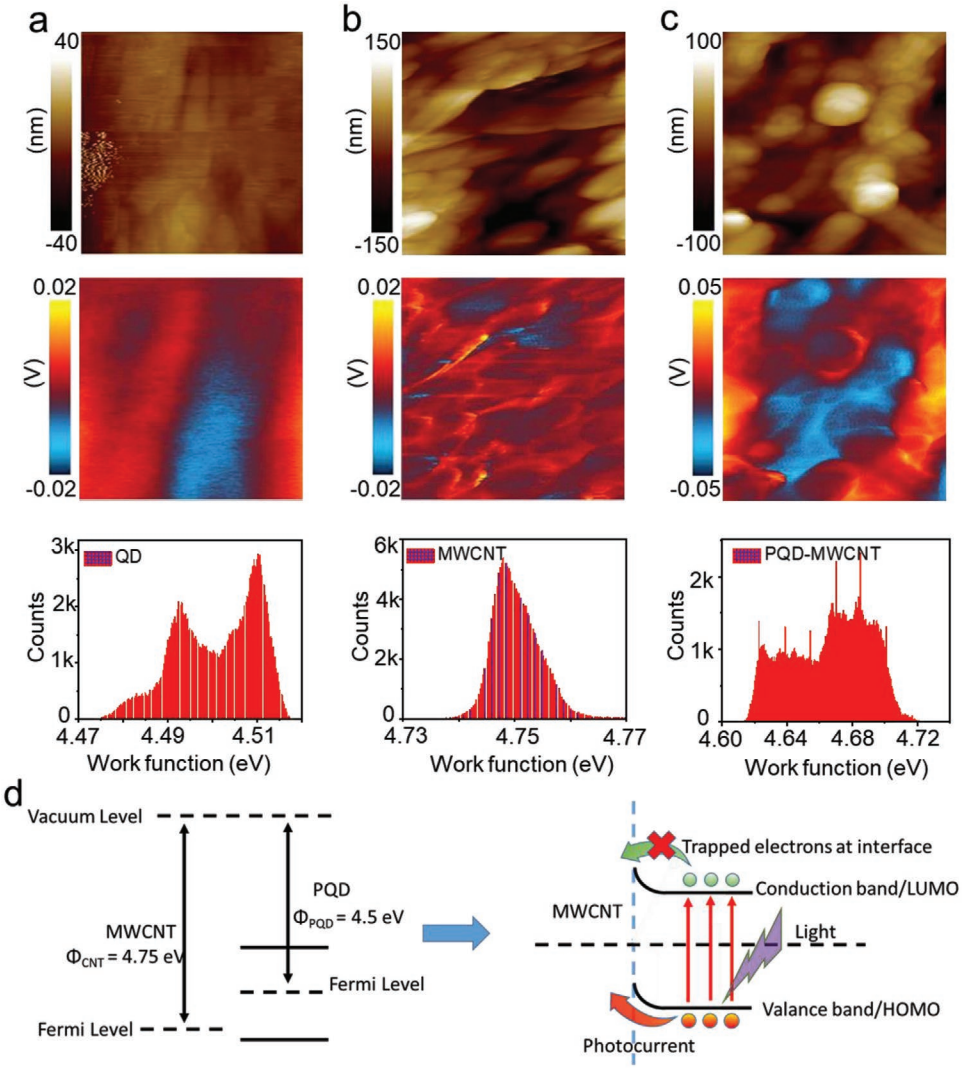

Figure 4. a–c) KPFM measurement of work function of PQD, MWCNT, and PQD-MWCNT films (the first row: AFM images (1 μm × 1 μm); the second row: corresponding KPFM images (1 μm × 1 μm); the third row: calculated work functions). d) The interface trapping mechanism of our PQD-MWCNT material.

The advantage of unsupervised machine learning compared to supervised machine learning is that the labeling process is not needed before training and the labeling could be done with a limited number of labeled data after training. Although the recognition rate in unsupervised machine learning is harder to achieve as high as supervised machine learning, the advantage of not requiring pretraining labels makes it adaptable for significant volumes of unknown natural data. After 40-epoch(round) training, the synaptic weights of our 50 output neurons (Figure 5c) indicate that our synapses catch some features of the training data. The accuracy is 52% with the test set. Due to the limitations of our measurement setup, the simulated accuracy is limited to 52%. It is mainly due to the limited number of pulses, as shown in Figure S9 in the Supporting Information, since the number of states of the device is directly related to the volume of *knowledge* the device is capable of remembering. Nonlinearity could also affect accuracy, as discussed earlier. However, large nonlinearity will result and decrease the accuracy if the number of pulses is increased to obtain more states. Therefore, for practical applications, to achieve higher accuracy for pattern recognition tasks, shorter pulses are preferred to reach an increase in the number of states while avoiding large nonlinearity of the synaptic weight change.

3. Conclusion

In summary, we have successfully combined the advantages of $MAPbBr_3$ PQDs and MWCNTs to make a new PQD-MWCNT hybrid material that was used to make a two-terminal device for neuromorphic computing. The PQD-MWCNT device shows excellent photoresponse compared to the previous research on CNT optoelectronic synapses.[8] The device shows a good light-induced memory effect from the interface charge trapping as revealed from the energy levels measured using KPFM analysis. The photonic memory mimics the strengthening of synaptic weight, in a way that is similarly observed in the biological brain. By varying intensities, pulse number, and pulse

© 2020 Wiley-VCH GmbH

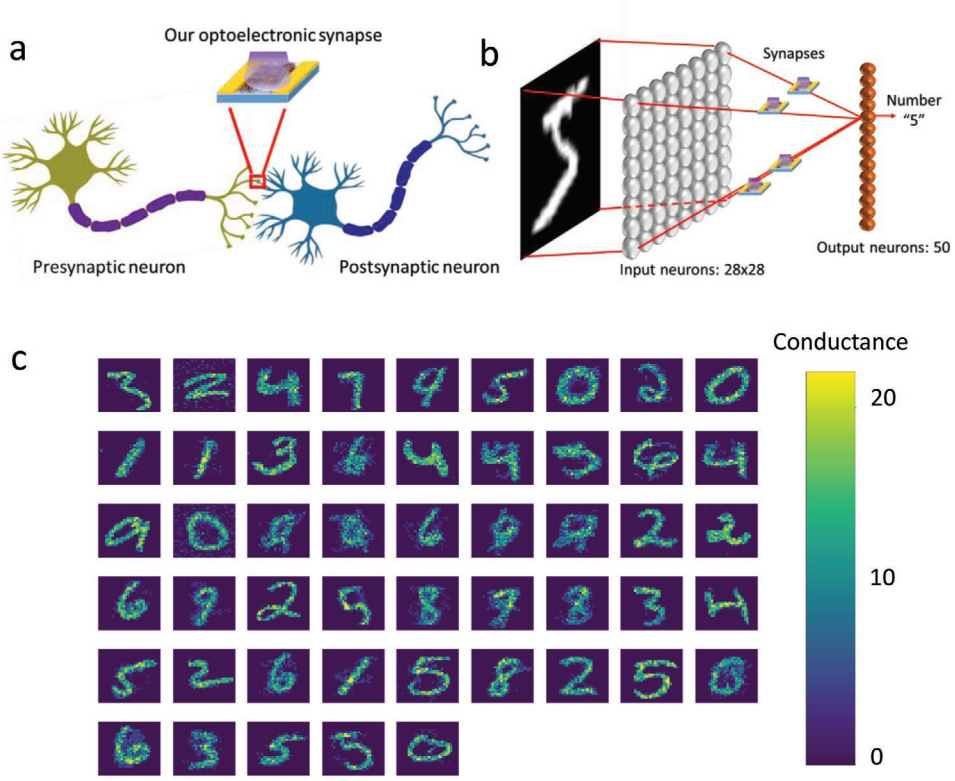

Figure 5. a) Schematic of interconnected synapses between a presynaptic neuron and a postsynaptic neuron. b) Simulation structure of the spiking neural network. c) Synaptic weights of each output neuron.

width, synaptic properties that emulate the biological brain were studied. These results are highly relevant for emerging neuromorphic computing applications. We also demonstrate the erasing of the memory (memory depression) by applying electrical pulses, which is also important in the neuromorphic learning process. Moreover, using the weight change properties of our optoelectronic synapses, pattern recognition simulation is performed to demonstrate that our device can act as building blocks in neuromorphic computers. Since our PQDs are grown on the wall of single MWCNT and each MWCNT after PQD growth acts as a single device to absorb light and transport electrons, our new hybrid material has great potential as a building block for future nanoscale or single MWCNT-based optoelectronic neuromorphic computing and sensing devices.

4. Experimental Section

PQD-MWCNT Hybrid Material Synthesis: First, 2 mg MWCNT (MWCNTs (>95%, outside diameter: 10–20 nm) from US Research Nanomaterials, Inc) was put in 6 mL Toluene and sonicated with a probe sonicator under 25% power for 1 min. Then 200 µL $MAPbBr_3$ precursor (17.3 mg MABr + 73 mg PbBr2 + 5 mL DMF + 300 µL butylamine + 500 µL oleic acid) was dropped into the MWCNT solution and the new MWCNT solution was sonicated for 5 min to initiate PQD growth. After sonication, it was waited for 30 min for the growth to be complete. After growth was complete, the washing process was repeated three times to purify the MWCNTs with PQDs from nongrown/solution grown PQDs. The washing process involved centrifugation of the solution at 3000 rpm for 10 min followed by separation of PQD-MWCNTs from PQD solution and redispersing it in toluene for the next washing. After purification, the solution was sonicated for 5 min to make MWCNTs well dispersed in the toluene for film making.

Device Fabrication: Films of PQD-MWCNTs and MWCNTs were formed using spin coating to test their photoresponse in a device. To make the film more uniform, a very thin film of polyvinyl alcohol (PVA) (10% water solution) was spin-coated with 3000 rpm spin speed before coating PQD-MWCNT. The microscope image of the PQD-MWCNT film is shown in Figure S10 in the Supporting Information. Thermal evaporation was used to deposit gold electrodes of the devices. The channel length between two gold electrodes is 50 µm and the width is 250 µm.

Material and Device Characterization: Absorbance spectra and PL spectra of both solution and films were measured by Agilent Cary UV–vis 300 and Horriba Nanolog FL3-11, separately. 405 nm excitation was used to obtain PL spectra. Renishaw RM 1000B Micro-Raman Spectrometer was used to measure Raman with 514 nm excitation source. XRD data were obtained by PANalytical Empyrean #2 with 1.8 KW Copper X-ray Tube. KPFM measurement was performed using NanoIR2 from Bruker with PR-EX-KPFM cantilevers and Platinum/Iridium coated tips.

The device measurement was performed by Keithley 2636B equipment by using Labview.

Supporting Information

Supporting Information is available from the Wiley Online Library or from the author.

Acknowledgements

J.T. acknowledges the National Science Foundation (CAREER: ECCS-1351757) for the financial support.

© 2020 Wiley-VCH GmbH

Conflict of Interest

The authors declare no conflict of interest.

Author Contributions

J.X.L. and P.D. contributed equally to this work. J.X.L. and P.D. prepared the PQD-MWCNT film and performed TEM, UV–vis, Raman and PL measurements. J.X.L. designed, fabricated, and conducted the optoelectronic synapse measurements with the help of P.D. J.X.L. analyzed Raman results and performed ML simulations for optoelectronic synapses. K.S.K. performed KPFM and XRD measurements and analyzed the results with the assistance of J.X.L. All the authors contributed to the discussion of the results and approved the paper. J.T. conceived the idea and directed the overall performance of the project.

Keywords

carbon nanotubes, neuromorphic computing, optoelectronic synapses, perovskite quantum dots, photonic memory

Received: May 25, 2020
Revised: September 14, 2020
Published online: November 5, 2020

[1] T. F. de Lima, B. J. Shastri, A. N. Tait, M. A. Nahmias, P. R. Prucnal, *Nanophotonics* **2017**, *6*, 577.
[2] J. Pei, L. Deng, S. Song, M. Zhao, Y. Zhang, S. Wu, G. Wang, Z. Zou, Z. Wu, W. He, *Nature* **2019**, *572*, 106.
[3] E. Moen, D. Bannon, T. Kudo, W. Graf, M. Covert, D. Van Valen, *Nat. Methods* **2019**, *16*, 1233.
[4] K. Noda, Y. Yamaguchi, K. Nakadai, H. G. Okuno, T. Ogata, *Appl. Intell.* **2015**, *42*, 722.
[5] R. Ramprasad, R. Batra, G. Pilania, A. Mannodi-Kanakkithodi, C. Kim, *npj Comput. Mater.* **2017**, *3*, 54.
[6] G. Rahman, Z. Najaf, A. Mehmood, S. Bilal, A. H. A Shah, S. A. Mian, G. Ali, *Carbon Nanotubes* **2019**, *5*, 3.
[7] a) M. M. Shulaker, G. Hills, N. Patil, H. Wei, H.-Y. Chen, H.-S. P. Wong, S. Mitra, *Nature* **2013**, *501*, 526; b) G. Hills, C. Lau, A. Wright, S. Fuller, M. D. Bishop, T. Srimani, P. Kanhaiya, R. Ho, A. Amer, Y. Stein, *Nature* **2019**, *572*, 595.
[8] G. Agnus, W. Zhao, V. Derycke, A. Filoramo, Y. Lhuillier, S. Lenfant, D. Vuillaume, C. Gamrat, J. P. Bourgoin, *Adv. Mater.* **2010**, *22*, 702.
[9] a) I. Ka, L. F. Gerlein, R. Nechache, S. G. Cloutier, *Sci. Rep.* **2017**, *7*, 45543; b) T.-F. Zhang, Z.-P. Li, J.-Z. Wang, W.-Y. Kong, G.-A. Wu, Y.-Z. Zheng, Y.-W. Zhao, E.-X. Yao, N.-X. Zhuang, L.-B. Luo, *Sci. Rep.* **2016**, *6*, 38569; c) J. Zheng, C. Luo, B. Shabbir, C. Wang, W. Mao, Y. Zhang, Y. Huang, Y. Dong, J. J. Jasieniak, C. Pan, *Nanoscale* **2019**, *11*, 8020; d) I. Ka, L. F. Gerlein, I. M. Asuo, R. Nechache, S. G. Cloutier, *Nanoscale* **2018**, *10*, 9044; e) F. Li, Z. Qiu, S. Liu, H. Zhang, *ACS Appl. Nano Mater.* **2019**, *2*, 4974.
[10] P. Bansal, X. Zhang, H. Wang, P. Kar, W. Yu, *Nanoscale Adv.* **2020**, *2*, 808.
[11] A. Kojima, K. Teshima, Y. Shirai, T. Miyasaka, *J. Am. Chem. Soc.* **2009**, *131*, 6050.
[12] M. I. Saidaminov, V. Adinolfi, R. Comin, A. L. Abdelhady, W. Peng, I. Dursun, M. Yuan, S. Hoogland, E. H. Sargent, O. M. Bakr, *Nat. Commun.* **2015**, *6*, 8724.
[13] C. Gu, J.-S. Lee, *ACS Nano* **2016**, *10*, 5413.
[14] B. Pradhan, S. Das, J. Li, F. Chowdhury, J. Cherusseri, D. Pandey, D. Dev, A. Krishnaprasad, E. Barrios, A. Towers, *Sci. Adv.* **2020**, *6*, eaay5225.
[15] Y. Wang, Z. Y. Lv, J. R. Chen, Z. P. Wang, Y. Zhou, L. Zhou, X. L. Chen, S. T. Han, *Adv. Mater.* **2018**, *30*, 1802883.
[16] a) H. Huang, F. Zhao, L. Liu, F. Zhang, X.-g. Wu, L. Shi, B. Zou, Q. Pei, H. Zhong, *ACS Appl. Mater. Interfaces* **2015**, *7*, 28128; b) S. S. Mali, C. S. Shim, C. K. Hong, *NPG Asia Mater.* **2015**, *7*, e208.
[17] D. Erdemir, A. Y. Lee, A. S. Myerson, *Acc. Chem. Res.* **2009**, *42*, 621.
[18] S. Xiong, W. Qi, B. Huang, M. Wang, L. Wei, *J. Phys. Chem. C* **2011**, *115*, 10365.
[19] Z. F. Zhao, L. Jing, Z. H. Wu, J. Cheng, M. M. Zhang, Y. F. Hou, *J. Mater. Sci.* **2018**, *53*, 15430.
[20] https://n.b5z.net/i/u/10091461/f/CNTs%20Linked%20Files/US4306_raman.pdf (accessed: October 2020).
[21] a) R. G. Niemann, A. G. Kontos, D. Palles, E. I. Kamitsos, A. Kaltzoglou, F. Brivio, P. Falaras, P. J. Cameron, *J. Phys. Chem. C* **2016**, *120*, 2509; b) T. Zhang, L. Xie, L. Chen, N. Guo, G. Li, Z. Tian, B. Mao, Y. Zhao, *Adv. Funct. Mater.* **2017**, *27*, 1603568.
[22] Y. Gao, X. Zhao, P. Yin, F. Gao, *Sci. Rep.* **2016**, *6*, 20539.
[23] A. K. Arora, M. Rajalakshmi, T. Ravindran, V. Sivasubramanian, *J. Raman Spectrosc.* **2007**, *38*, 604.
[24] a) P. Bansal, Y. Khan, P. Kar, *New J. Chem.* **2019**, *43*, 4116; b) H. Mashiyama, Y. Kawamura, Y. Kubota, *J. Korean Phys. Soc.* **2007**, *51*, 850.
[25] F. Chen, C. Xu, Q. Xu, Y. Zhu, F. Qin, W. Zhang, Z. Zhu, W. Liu, Z. Shi, *ACS Appl. Mater. Interfaces* **2018**, *10*, 25763.
[26] C.-C. Chang, P.-C. Chen, T. Chou, I.-T. Wang, B. Hudec, C.-C. Chang, C.-M. Tsai, T.-S. Chang, T.-H. Hou, *IEEE J. Emerging Sel. Top. Circuits Syst.* **2017**, *8*, 116.
[27] Z. Ni, Y. Wang, L. Liu, S. Zhao, Y. Xu, X. Pi, D. Yang, presented at 2018 IEEE Int. Electron Devices Meet. (IEDM) (IEEE), Hilton San Francisco Union Square, December **2018**.
[28] P. Greengard, *Science* **2001**, *294*, 1024.
[29] L. A. Algharagholy, *J. Electron. Mater.* **2019**, *48*, 2301.
[30] L. Adamska, G. V. Nazin, S. K. Doorn, S. Tretiak, *J. Phys. Chem. Lett.* **2015**, *6*, 3873.
[31] W. Melitz, J. Shen, A. C. Kummel, S. Lee, *Surf. Sci. Rep.* **2011**, *1*, 66.

 © 2020 Wiley-VCH GmbH